MATERIALS ENGINEERING

Ultralight, scalable, and high-temperature–resilient ceramic nanofiber sponges

Haolun Wang,[1,2]* Xuan Zhang,[3]* Ning Wang,[1†] Yan Li,[3] Xue Feng,[3] Ya Huang,[2] Chunsong Zhao,[2] Zhenglian Liu,[4] Minghao Fang,[4] Gang Ou,[2,5] Huajian Gao,[6†] Xiaoyan Li,[3†] Hui Wu[2†]

Ultralight and resilient porous nanostructures have been fabricated in various material forms, including carbon, polymers, and metals. However, the development of ultralight and high-temperature resilient structures still remains extremely challenging. Ceramics exhibit good mechanical and chemical stability at high temperatures, but their brittleness and sensitivity to flaws significantly complicate the fabrication of resilient porous ceramic nanostructures. We report the manufacturing of large-scale, lightweight, high-temperature resilient, three-dimensional sponges based on a variety of oxide ceramic (for example, TiO_2, ZrO_2, yttria-stabilized ZrO_2, and $BaTiO_3$) nanofibers through an efficient solution blow-spinning process. The ceramic sponges consist of numerous tangled ceramic nanofibers, with densities varying from 8 to 40 mg/cm^3. In situ uniaxial compression in a scanning electron microscope showed that the TiO_2 nanofiber sponge exhibits high energy absorption (for example, dissipation of up to 29.6 mJ/cm^3 in energy density at 50% strain) and recovers rapidly after compression in excess of 20% strain at both room temperature and 400°C. The sponge exhibits excellent resilience with residual strains of only ~1% at 800°C after 10 cycles of 10% compression strain and maintains good recoverability after compression at ~1300°C. We show that ceramic nanofiber sponges can serve multiple functions, such as elasticity-dependent electrical resistance, photocatalytic activity, and thermal insulation.

INTRODUCTION

Three-dimensional (3D) resilient nanostructures, such as graphene monoliths (*1*, *2*), carbon nanotube aerogels (*3*), polymer foams (*4*), and metal microlattices (*5*, *6*), have been synthesized and explored for a wide range of applications, including tissue engineering, thermal insulation, energy storage, filtration, and environmental protection (*7*–*10*). Although these 3D nanostructures generally exhibit superior properties, including high porosity, large surface area, reliable mechanical properties, and ultralow density (*11*, *12*), applications at high temperatures in air still remain challenging because of their relatively unstable constituent materials (carbon, polymers, and metals). In contrast, ceramics feature high strength and good mechanical/chemical stability at high temperatures (*13*, *14*), but their brittleness and flaw sensitivity have so far limited the development of lightweight and resilient ceramic systems (*15*, *16*).

Microarchitectural cellular structures made of nanoceramics (*17*) and nanoceramic composites (*18*) are typically brittle despite many superior properties, including substantially enhanced specific stiffness and strength. More recently, a compelling hollow-tube alumina nanolattice structure, with tube wall thickness of 5 to 60 nm, tube major axis around 1 μm, and whole-cell width of 25 to 75 μm, has been recently fabricated based on two-photon lithography direct laser writing (DLW), atomic layer deposition, and oxygen plasma etching (*19*). Deformation in this nanolattice appears to be dominated by elastic buckling of the tube shell, leading to substantial ductility and good recoverability under uniaxial compression at room temperature. However, this nanolattice is generally limited to below 1 mm in size and cannot easily scale up to larger systems because of its DLW-based synthesis process. Nanoporous monolithic alumina and lanthanide oxide aerogels (*20*–*23*) have been synthesized via sol-gel and self-assembly methods. These aerogels exhibit ultralow density and excellent thermal properties, but their specific modulus and strength are much lower than those of nanolattices (*19*). To date, there has been no investigation on the high-temperature resilience of lightweight ceramic cellular structures.

It has recently been recognized that ceramic nanocrystalline nanofibers are highly flexible because of their high aspect ratios and nanometer-sized grains (*24*, *25*) and can be an ideal candidate for building blocks for 3D elastic assemblies (*26*). A variety of ceramic nanofibers have been successfully prepared through electrospinning, which uses an electric field to draw fibers from precursor solutions (*27*). However, electrospun nanofibers typically form a thin film network of random or oriented nanofibers and cannot be easily assembled into large-scale 3D networks because of intrinsic limitations in the electrospinning technique. Here, we report the manufacturing of large-scale 3D sponges based on a variety of ceramic [for example, TiO_2, ZrO_2, yttria-stabilized ZrO_2 (YSZ), and $BaTiO_3$] nanofibers through an economic and efficient blow-spinning technique. Quantitative mechanical testing indicated that the nanofiber sponges exhibit excellent resilience at both room and high temperatures up to 800°C, and we also observed mechanical resilience of the YSZ nanofiber sponge at even higher temperatures (~1300°C). The ceramic nanofiber sponges also exhibit ultralow density, superior mechanical/chemical stability, efficient energy absorption during cyclic loading, and multifunctionalities, such as elasticity-dependent electrical resistance, photocatalytic activity, and thermal insulation.

RESULTS

Synthesis and structural characterization of ceramic nanofiber sponges

We developed a solution blow-spinning technique to fabricate ceramic nanofibers and assemble them into 3D nanofiber sponges. Compared to

---

[1] State Key Laboratory of Electronic Thin Films and Integrated Devices, University of Electronic Science and Technology of China, Chengdu 610054, China. [2] State Key Laboratory of New Ceramics and Fine Processing, School of Materials Science and Engineering, Tsinghua University, Beijing 100084, China. [3] Centre for Advanced Mechanics and Materials, Applied Mechanics Laboratory, Department of Engineering Mechanics, Tsinghua University, Beijing 100084, China. [4] School of Materials Science and Technology, China University of Geosciences, Beijing 100083, China. [5] Department of Chemistry and Collaborative Innovation Center for Nanomaterial Science and Engineering, Tsinghua University, Beijing 100084, China. [6] School of Engineering, Brown University, Providence, RI 02912, USA.
*These authors contributed equally to this work.
†Corresponding author. Email: huiwu@tsinghua.edu.cn (H. Wu); Huajian_Gao@brown.edu (H.G.); xiaoyanlithu@tsinghua.edu.cn (X.L.); ning_wang@uestc.edu.cn (N.W.)

electrospinning, our present technique has the advantage of much higher (by several times) fiber production rate and the freedom to dispense with a high-voltage electric field (*28*). Moreover, for a precursor with a relatively high concentration of inorganic salts, a "jam" phenomenon near the tip of the syringe needle usually occurs during electrospinning because the electrical conductivity of the precursor rises with the addition of inorganic salts, causing an instability in the electrospinning process. In comparison, for blow-spinning, the precursor with these high concentration salts can be spun with ease. If the precursor solutions in electrospinning and blow-spinning are similar, there is no significant difference in the yield rate, aspect ratio, and grain size of the nanofiber. Details of the synthesis process are given in Materials and Methods. As illustrated in Fig. 1A and fig. S1, a precursor solution is pumped through an inner muzzle with a diameter of 0.16 mm, and, simultaneously, air flows through a concentric outer nozzle with a diameter of 1 mm. The precursor solution is naturally stretched by the air flow and solidified to fibers with diameters of hundreds of nanometers associated with solvent evaporation. The ejected nanofibers were concentrated in an air-permeable cage-like collector to form a highly porous sponge. The method is highly efficient and can be scaled up, allowing us to obtain a macro-sized $Ti(OBu)_4$/polyvinylpyrrolidone (PVP) nanofiber sponge in a short time, as shown in Fig. 1B. After calcination for 200 min at 450°C, the PVP is removed, and $Ti(OBu)_4$ is then hydrolyzed into pure TiO_2 sponges with ultralow density (Fig. 1C), typically ranging from 8 to 40 mg/cm^3, depending on the fiber diameter and sponge porosity. This density range is comparable to that of ceramic aerogels (*26*) and nanolattices (*19*). The ceramic nature of the nanofibers allows the sponge to withstand high-temperature flames without any visible damage and deformation (Fig. 1D).

The average diameter of the nanofibers can be controlled from 47 to 815 nm by controlling the concentration of the precursor solutions (fig. S2). Figure 1E shows a scanning electron microscopy (SEM) image of a piece of TiO_2 sponge, where uniform nanofibers with a diameter of ~180 nm interweave with each other, leading to a cellular architecture with open-cell geometry and porosity above 99.7% (Fig. 1F). Figure 1G shows a TEM image of a TiO_2 nanofiber. In combination with the traditional sol-gel process, our synthesis process can be easily extended to other ceramic materials. For example, we have applied the solution blow-spinning technique to fabricate ZrO_2, YSZ, and $BaTiO_3$ nanofiber sponges (figs. S3 to S5).

Compressive behavior of ceramic nanofiber sponges at room temperature

The ceramic nanofiber sponges can be repeatedly compressed to large strains, with marked recoverability after each compression, as shown in Fig. 2A, fig. S6, and movie S1. To reveal the underlying mechanism, we performed in situ monotonic and cyclic uniaxial compression tests inside an SEM on the nanofiber sponges at both room temperature and 400°C via a Hysitron PI 85 PicoIndenter assisted with a heating device. Quantitative compressive testing at higher temperatures (for example, 400°, 600°, and 800°C) was carried out via a Hysitron TI 950 TriboIndenter. More details of the testing procedure are supplied in Materials and Methods. Hundreds of micrometer-sized specimens manufactured from macroscopic nanofiber sponges were used for

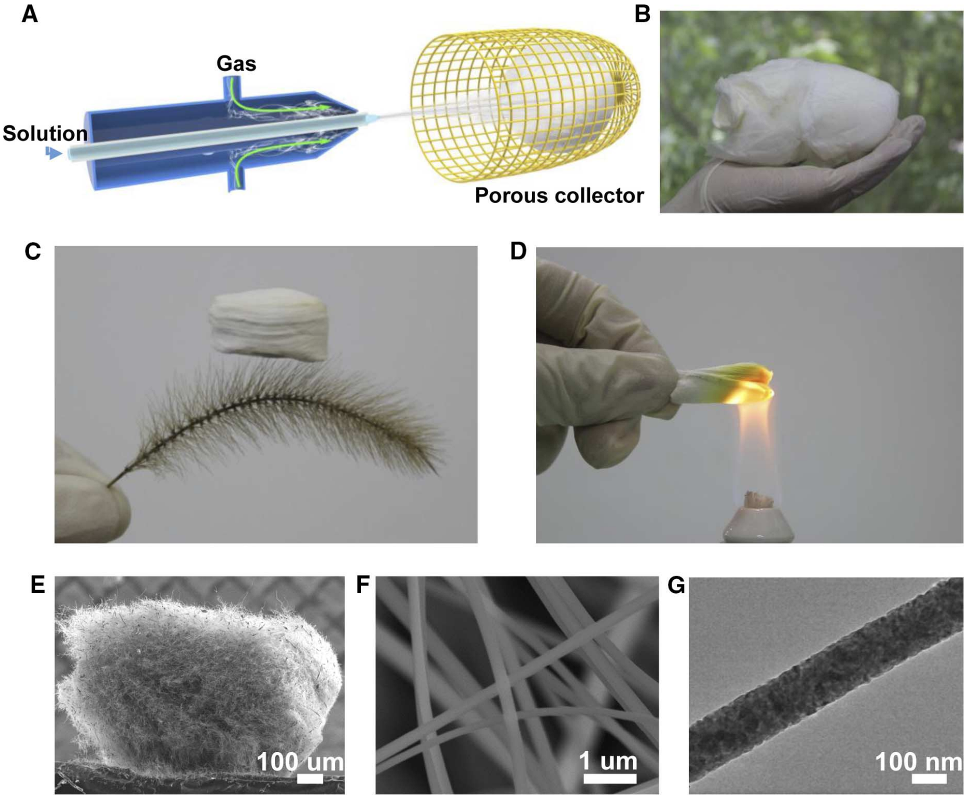

Fig. 1. Synthesis and structural characterization of TiO_2 nanofiber sponge. (**A**) Schematic of a solution blow-spinning. (**B**) Photograph of a macro-sized $Ti(OBu)_4$/PVP precursor sponge. (**C**) Ultralight TiO_2 sponge standing on a setaria viridis. (**D**) Sponge heated by an alcohol lamp without damage, indicating good heat resistance. (**E**) SEM image of millimeter-sized TiO_2 sponge. (**F**) Zoomed-in section of TiO_2 sponge. The image shows the cellular fibrous structure and the uniform distribution of nanofibers. (**G**) Transmission electron microscopy (TEM) image of a TiO_2 nanofiber.

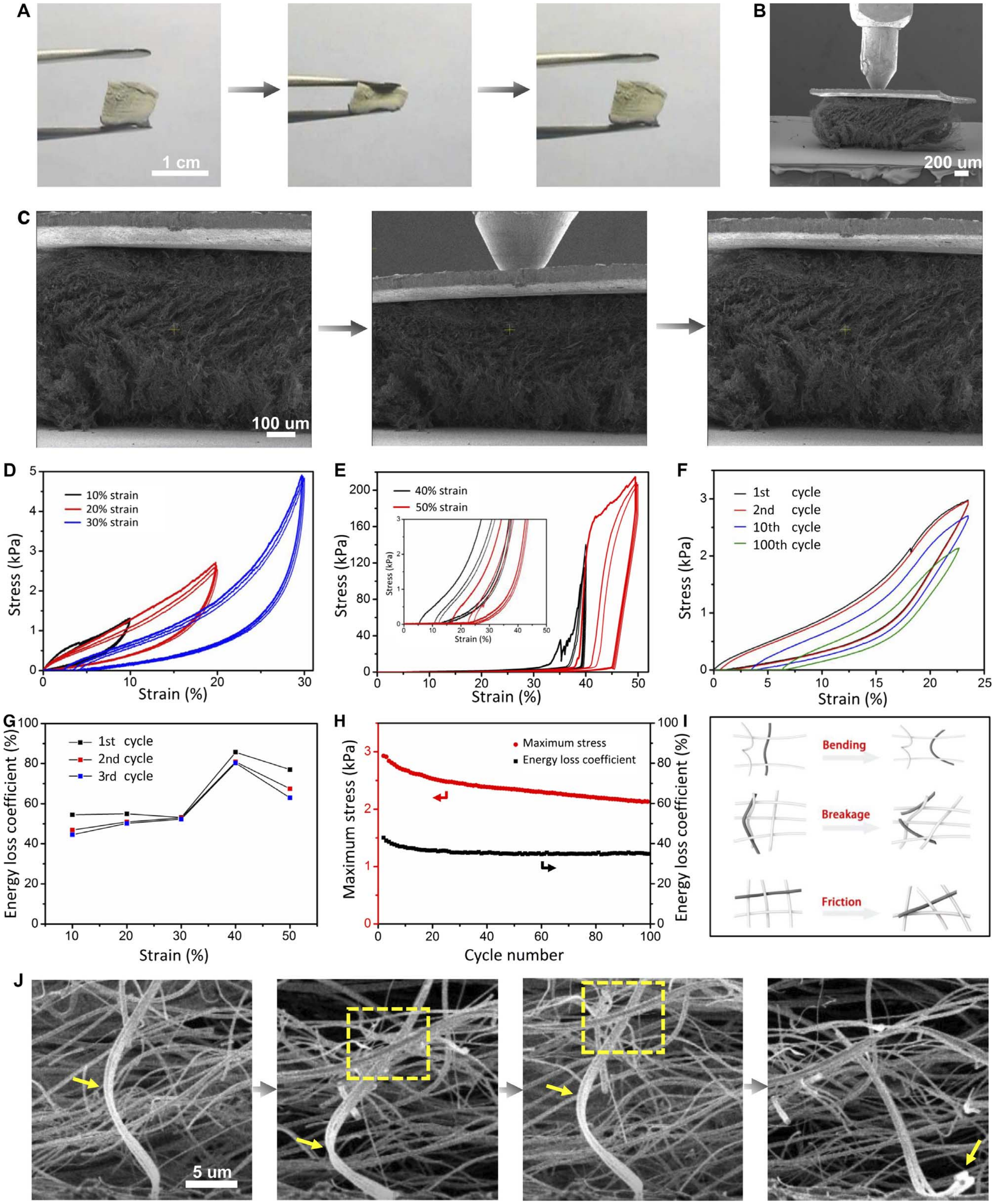

Fig. 2. Compressive test results of TiO_2 nanofiber sponge with a density of ~35 mg/cm^3 at room temperature. (**A**) Compression and recovery processes of macroscopic TiO_2 sponge. (**B**) SEM image of TiO_2 sponge pressed by a nanoindenter. (**C**) In situ SEM images of compressive process of TiO_2 sponge. (**D** and **E**) Cyclic compressive stress-strain curves of TiO_2 sponge under 10 to 50% strain. Each test was repeated for three cycles, and the inset shows the magnification of initial part of curves in (E). (**F**) Cyclic compressive stress-strain curves of TiO_2 sponge under 23% strain for 100 cycles. (**G**) Energy loss coefficient of sponge compressed for three cycles by 10 to 50% strain in (D) and (E). (**H**) Variation of energy loss coefficient and maximum stress with cycle number of TiO_2 sponge in (F). (**I**) Schematic of energy dissipation mechanisms. (**J**) Zoomed-in SEM images during the compression process, showing the bending and springback of a hank of nanofibers and the friction of neighboring nanofibers, and the fourth picture shows their breakage after some cycles.

mechanical testing. During testing, the specimen was glued via a silver paste between the Si loading stage and a light metal sheet and was subjected to compression by a conical nanoindenter with a 100-μm-diameter flat tip (Fig. 2, B and C). Figure 2D shows a series of cyclic compressive stress-strain curves of a TiO_2 sponge with a density of ~35 mg/cm^3 at room temperature under different strains of 10, 20, and 30%. From the linear elastic regime of the stress-strain curve during the first cycle of compression, the compressive modulus of the TiO_2 sponge is estimated to be about 12.25 kPa. Figure S7 shows the compressive modulus as a function of relative density of our ceramic nanofiber sponges and other available porous materials in previous studies. The compressive modulus of our sponges follows the scaling law $E \sim (\rho/\rho_s)^2$ with respect to the relative density, similar to nanofibrous aerogels made up of polyacrylonitrile and SiO_2 nanofibers. This indicates that the ceramic nanofiber sponge is an open-cell bending-dominated structure. Furthermore, our ceramic sponge is capable of retaining its stiffness and resilience even at high temperatures, suggesting potential applications of the sponge in an extreme environment. It was observed that the sponge can almost recover to its original shape when released from different compressive strains of 10 to 30%. Figure 2C shows a sequence of SEM snapshots of the sponge structure during loading and unloading cycles. These images reveal a number of typical deformation mechanisms during compression and recovery, including the bending and springback of individual nanofibers, narrowing and recovery of micrometer-sized pores, and relative motion between neighboring nanofibers (Fig. 2C and movie S2). As the sponge is compressed to 40 and 50% strain, there exist apparent stress fluctuations in the first cycle of the stress-strain curve. The stress fluctuation corresponds to discrete failure events, that is, some nanofibers undergo irreversible deformation or fracture, leading to permanent damage of the structure. After the first cycle compression to 40% strain, the sponge recovered to 89% of its original height. Although there exists some damage after the first cycle, the peak stresses in the subsequent cycles remain almost the same (Fig. 2E), indicating that local failure of some nanofibers does not significantly influence the carrying capacity of the overall sponge (*29*). As the strain is increased beyond 35%, the stress rose steeply, and the maximum stress reached up to 200 kPa at 50% strain (Fig. 2E). This rapid rise in stress is apparently induced by the densification of the structure and increased friction between neighboring nanofibers upon severe volume reduction (*3*). The compressive strength at 50% strain of the TiO_2 sponge is higher than those of metallic microlattices (*5*), polymer foams (*4*), and carbon-based foams (*30*) at similar densities. After 100 cycles of compression at 23% strain and room temperature, the TiO_2 sponge exhibited a residual strain of only 7% and a maximum stress nearly 73% of its original value (Fig. 2F and fig. S8). A macroscopic specimen of the TiO_2 sponge with a density of 8.5 mg/cm^3 exhibited a residual strain of only 13% and a maximum stress nearly 90% of its original value after 100 cycles of cyclic compression at 50% strain and room temperature, which further illustrated the excellent resilience of the TiO_2 sponge (fig. S9 and movie S3).

Energy absorption or dissipation is one of the crucial functions of porous nanostructures (*4*). The TiO_2 sponge also exhibited significant hysteresis during compression. At the first cycle of compression to 50% strain (Fig. 2E), the total work done per unit volume is estimated to be about 38.1 mJ/cm^3, and the dissipated energy density is about 29.6 mJ/cm^3, leading to an energy loss coefficient of about 77.8%. This dissipated energy density is higher than those of recently reported cellular structures (*5*, *30*, *31*). The observed large energy dissipation mainly results from the plastic deformation, fracture of nanofibers, and friction between adjacent nanofibers. Figure 2G summarizes the energy loss coefficients associated with the first three cycles shown in Fig. 2 (D and E). As the maximum applied strain increases from 10 to 40%, the energy loss coefficient increases from 50 to 80%, which is comparable to that of aerogels and other cellular structures (*5*, *31*, *32*). The slight decrease in energy loss coefficient at 50% strain is due to the extensive damage of structure in the first cycle. Figure 2H plots the variation of the maximum stress and energy loss coefficient during 100 compressive cycles shown in Fig. 2F. The maximum stress slightly decreases with the cycle number, but the energy loss coefficient first decreases and then remains constant at about 37% after 10 cycles. In previous studies on metallic and ceramic hollow-tube lattices, energy absorption was achieved through fracture and buckling of tube walls (*5*, *19*). For the ceramic nanofibrous sponge under study, the energy absorption mechanisms include plastic deformation and/or fracture of individual nanofibers as well as friction between adjacent nanofibers, as illustrated in Fig. 2I and SEM details in Fig. 2J.

Compressive testing of ceramic nanofiber sponges at high temperatures

A vast majority of cellular structures have been made from polymers, metals, and carbon, exhibiting excellent mechanical properties at room temperature (*2*, *4*, *5*, *33*). However, these constituent materials typically cannot stand high temperatures. In contrast, ceramics are excellent heat resistant materials. As demonstrated in Fig. 3A, fig. S10, and movie S4, TiO_2, ZrO_2, and $BaTiO_3$ sponges exhibit good recoverability after compression in the flame of an alcohol lamp. We further conducted quantitative compressive testing on the fabricated ceramic sponges at high temperatures of 400° to 800°C. During in situ SEM experiments, the TiO_2 sponge was first heated to 400°C via microelectromechanical systems (MEMS) heating device integrated in the PI 85 stage (Fig. 3B). The specimen was then subjected to cyclic compression (Fig. 3C and movie S5) at the target temperature. Figure 3D plots a series of cyclic compressive stress-strain curves of a TiO_2 sponge with a density of ~40 mg/cm^3 at 400°C. These curves with a maximum strain of about 23% show a residual strain of only 5% at 400°C after 10 cycles. Meanwhile, the dissipated energy density at the first cycle was estimated to be 1.52 mJ/cm^3, and the variation of the maximum stress and energy loss coefficient with the cycle number is displayed in Fig. 3E. These mechanical properties are close to those of the sponge at room temperature shown in Fig. 2F, indicating that the TiO_2 nanofiber sponges retain their high resilience (or good recoverability) and high energy dissipation properties at 400°C. In particular, the YSZ sponge was heated in a methane flame for 10 min without shrinkage and cracking (Fig. 3F). The temperature of the methane flame is between 1184° and 1479°C (fig. S11). The YSZ sponges exhibit good recoverability after a number of compression cycles under this high-temperature methane flame, as shown in movies S6 and S7. We also conducted cyclic compression of ZrO_2 sponges at 400°, 600°, and 800°C via a Hysitron TI 950 with a heating stage. Because of the limited displacement range in this instrument, the maximum strain is capped at about 10%. The measured compressive stress-strain curves in Fig. 3G and fig. S12 indicate that the specimens recover almost completely after compression, with residual strains of only ~1% at 800°C after 10 cycles, demonstrating excellent resilience of the YSZ sponge at 400° to 800°C under cyclic compression.

Influence of gain size on the resilience of sponges

In the above mechanical tests, the ceramic nanofibers in the fabricated nanofibrous sponges have a mean grain size of around 10 nm. These

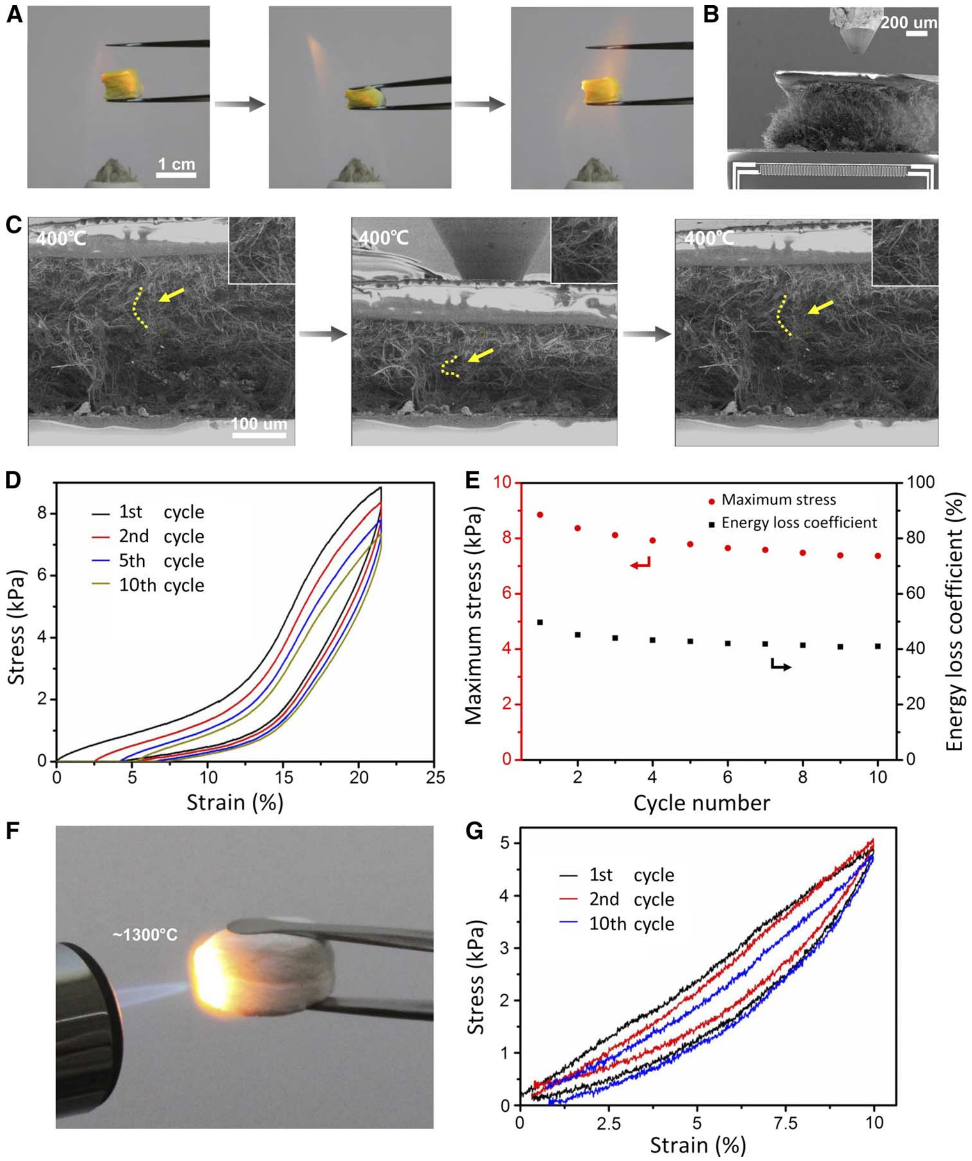

Fig. 3. Compressive test results of nanofiber sponge at high temperatures. (**A**) Compression and recovery processes of macroscopic TiO_2 sponge in the flame of an alcohol lamp. (**B**) SEM image of TiO_2 sponge pressed by a nanoindenter on the loading stage with a MEMS heating system. (**C**) In situ SEM images of compressive process of TiO_2 sponge at 400°C. The insets show the bending and springback of single nanofiber remarked in (C). (**D**) Stress-strain curves of TiO_2 sponge with a density of ~40 mg/cm^3 at 400°C for 10 cycles. (**E**) Variation of energy loss coefficient and maximum stress with cycle number of TiO_2 sponge in (D). (**F**) YSZ sponge heated by a methane flame. (**G**) Stress-strain curves of YSZ sponge at 800°C for 10 cycles.

nanocrystalline nanofibers are highly flexible and capable of bearing large elastic deformation, contributing to the high resilience of the nanofibrous sponges. We further investigated the influence of the mean gain size of nanofiber on the resilience of a whole sponge. We increased the sintering temperature of the $Ti(OBu)_4$/PVP sponges from 450° to 650°C to realize grain growth in the nanofibers. In this process, the crystalline structure transformed from a pure anatase to a rutile-anatase mixed structure (fig. S13). An analysis of the full width of the anatase peak at half maximum showed that the grain size increased from ~11 to ~34 nm, which is consistent with our observations in TEM (Fig. 1G and fig. S14). The same in situ SEM cyclic compression tests were performed on large-grained nanofiber sponges. Figure S15 shows the compressive stress-strain curves of a large-grained sponge with a density of ~30 mg/cm^3. There exist a number of apparent stress drops in these stress-strain curves, which are distinct from those of the small-grained sponges shown in Fig. 2F. Each stress drop corresponds to a discrete brittle failure event of some nanofibers, indicating that large-grained fibers are more brittle than small-grained ones. Although a number of large-grained nanofibers in the sponge fractured during compression, the recoverability and maximum stress of the whole sponge were not significantly affected. After 10 cycles, the large-grained nanofiber sponge still retained 97% of the original height and 90% of the maximum stress in the first cycle, which are comparable to those of the small-grained nanofiber sponges. This phenomenon may be attributed to the presence of numerous interlaced nanofibers, which provide support for the structure, even when some nanofibers suffer from brittle and catastrophic failure. These results indicate that the ceramic nanofibrous sponges have good structural stability.

Multifunctionality of ceramic nanofiber sponges

Because TiO_2 and ZrO_2 are two typical functional ceramic materials, one may wonder about the multifunctionalities of sponges made from these two materials. Figure 4 (A and B) shows the variation of normalized electrical resistance (R_t/R_0) of the TiO_2 sponge repeatedly compressed to 50% strain at room temperature and 30% strain at 400°C for 10 cycles, respectively. At room temperature, the value of R_t/R_0 decreases by about 65% under 50% compressive strain and recovers well after the load is released. Similarly, at 400°C, the value of R_t/R_0 decreases by 35% under 30% compressive strain and nearly recovers to the original value after unloading. This elasticity-dependent electrical resistance suggests the creation of numerous new temporary contacts among nanofibers during compression, leading to a large increase in conduction paths throughout the sponge, which decreases the electrical resistance (*26*). As shown in Fig. 4 (A and B), the response of R_t/R_0 only shows a slight change over multiple cycles of compression at both room temperature and 400°C, demonstrating promising stability of the structure and electrical properties at high temperatures.

TiO_2 is a well-known photocatalytic material with extraordinary abilities to degrade organic matter (*34*). However, TiO_2 powder is difficult to recycle after being dispersed in the solution for photocatalytic activity. Our ultralight and porous TiO_2 sponge is a convenient alternative that not only catalytically degrades organic matter, but also can be recycled easily. The TiO_2 sponge also has distinctive water absorption properties: A 2.1-mg sponge is capable of absorbing 107.8 mg of water, over 50 times its original mass (fig. S16), while still maintaining its structure and elasticity (fig. S17). After the sponge was dyed with organic stains, such as rhodamine B, the color of the sponge quickly faded (15 min) under illumination, as evidenced by Fig. 4C. The TiO_2 sponge can be immediately stained again and fade repeatedly under illumination without any other treatments for many cycles. This self-fading sponge, which has a stable structure and can be used repeatedly, has various potential applications in water purification and photocatalytic devices.

Because of their high porosity, porous cellular structures generally are excellent thermal insulation materials with low thermal conductivity. The thermal conductivity of the ZrO_2 nanofiber sponge (0.027 W/m·K at room temperature) is lower than that of most thermal insulation foams (table S1), indicating its superior thermal insulation performance.

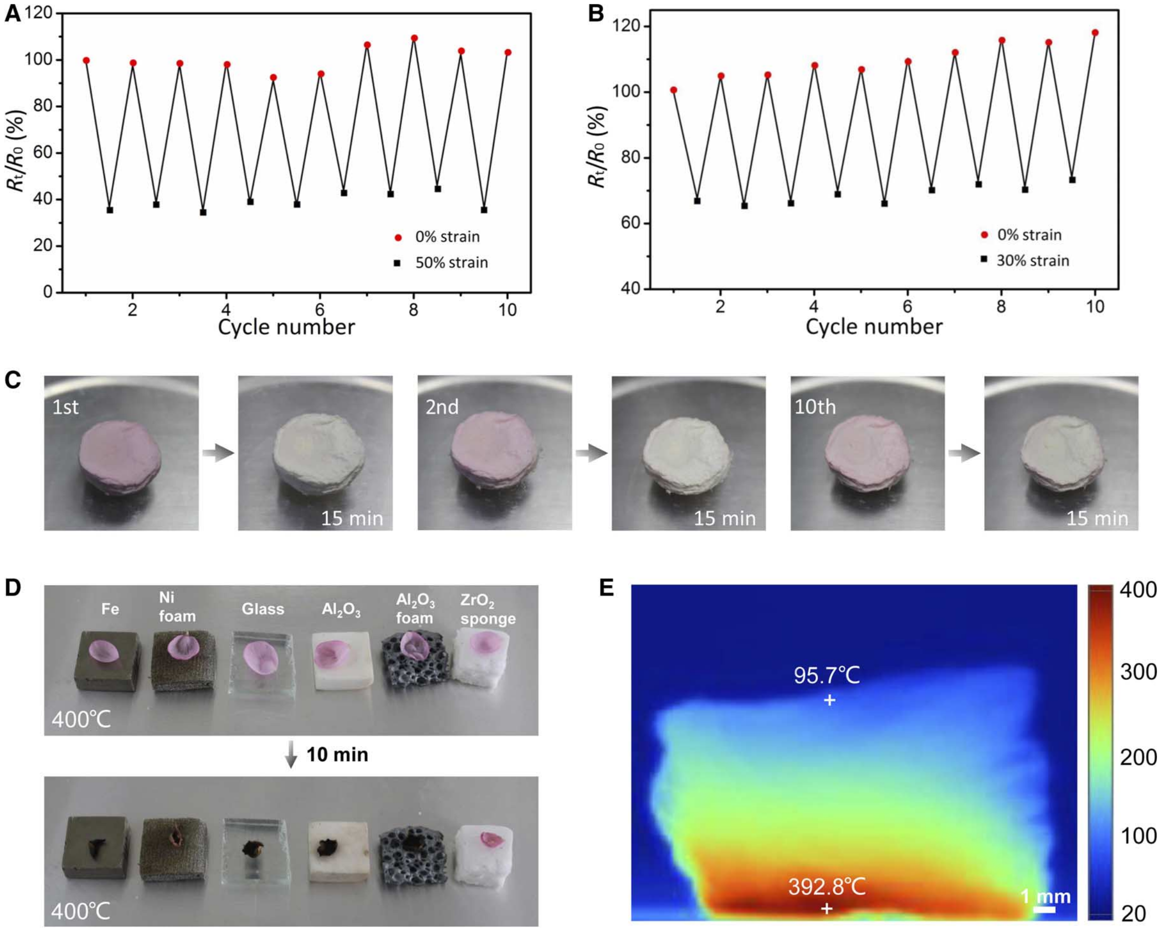

Fig. 4. Multifunctionality of ceramic nanofiber sponges. (**A** and **B**) Normalized electrical resistance change of TiO_2 sponges repeatedly compressed by 50% strain at room temperature and by 30% strain at 400°C for 10 cycles. (**C**) TiO_2 sponge dyed by rhodamine B and faded after illumination for 15 min. The photocatalysis process was repeated for many cycles. (**D**) High-temperature insulation capacity of ZrO_2 sponge. The ZrO_2 sponge effectively protects the fresh petal from withering, whereas petals on other materials were already carbonized on the 400°C heating stage after 10 min. (**E**) Infrared image of ZrO_2 sponge on a 400°C heating stage for 1 hour.

As illustrated in Fig. 4D, fresh flower petals were placed on top of 7-mm-thick plates made of iron, nickel foam, glass, Al_2O_3 ceramic, Al_2O_3 porous ceramic, and ZrO_2 nanofiber sponge on a 400°C heating stage. After 10 min, the petal on the ZrO_2 sponge exhibited only slight wilting, whereas other petals were carbonized. We monitored the temperature change on the top surface of these materials with time (fig. S18). The surface temperature of the ZrO_2 sponge only increased from 25° to 108°C, much lower than that of other materials. The infrared image in Fig. 4E illustrates that the top surface of the ZrO_2 sponge with a thickness of 1 cm maintained a relatively low temperature of about 95°C after being placed on a 400°C heating stage for 1 hour. These results indicate that the ZrO_2 sponge is an excellent thermal insulation material, which may be attributed to both the high porosity of the structure and the low thermal conductivity of ZrO_2.

DISCUSSION

In conclusion, we synthesized centimeter-sized and lightweight ceramic (TiO_2, ZrO_2, YSZ, and $BaTiO_3$) nanofiber sponges through an economic and efficient blow-spinning technique. These ceramic sponges displayed ultralow density, high resilience, and energy absorption. It has been shown that these sponges can maintain good recoverability after cyclic compression at temperatures above 400°C, which is challenging to other porous ceramic materials. They also have multiple functions, such as elasticity-dependent electrical conductivity, photocatalytic activity, and thermal insulation, with a broad range of potential applications in dampers, electrodes, heat insulators, absorbents, separators, and pressure sensors at high temperatures. The properties and functionalities of nanofibrous sponges are closely related to their microstructural parameters, including porosity, fiber diameter, and mean grain size of the fiber. The successful fabrication of these unique ceramic sponges provides new insights into the design and development of porous cellular structures for high-temperature applications.

MATERIALS AND METHODS

Preparation of ceramic nanofiber sponges

TiO_2 sponge

The precursor solution was prepared through the following procedure. Tetrabutyl titanate [$Ti(OBu)_4$] and PVP (M_w = 1,300,000) with a 2:1 mass ratio were mixed with ethanol and acetic acid at a mass ratio of 3:1. The solution was magnetically stirred for ~6 hours in a capped bottle at room temperature. The mixture was loaded into a 1-ml syringe with a specific coaxial needle. The precursor solution with 7 weight % (wt %) of PVP was injected from the axle with a speed of 3 ml/hour toward a porous and air-permeable cage collector placed at a distance of 20 cm, under a gas pressure of 69 kPa (airflow velocity is about 21 m/s at the exit) from the outer shaft. After spinning for 20 min at room temperature, a sponge of $Ti(OBu)_4$/PVP was obtained in the cage. The $Ti(OBu)_4$/PVP sponge was immediately treated at a heating rate of 2°C/min and then held at 450°C in air for 200 min before being cooled down in the furnace. After sufficient heating time, the grain size of the ceramic nanofiber only showed slight changes at the experimental temperatures, which were lower than the heating temperature during fabrication. This avoids the influence of grain growth on deformation of sponges at high temperatures.

ZrO_2 sponge

Zirconium oxychloride ($ZrOCl_2 \cdot 8H_2O$) and PVP with a 2:1 mass ratio were mixed with ethanol and deionized water at a mass ratio of 1:1. The solution was then magnetically stirred for ~6 hours in a capped bottle at room temperature. The spinning process was the same as that for the TiO_2 sponge. The sponge was then treated at a heating rate of 2°C/min with a holding time of 200 min at a temperature of 800°C in air and then cooled in the furnace. The precursor solution of YSZ was fabricated by zirconium *n*-propoxide, yttrium nitrate, PVP, diacetone, and ethanol.

$BaTiO_3$ sponge

Barium acetate [$Ba(Ac)_2$] was dissolved in acetic acid, and $Ti(OBu)_4$ was then added drop by drop with continuous stirring. After dissolution, 7 wt % of PVP and ethanol was added into the solution [the molar ratio of $Ba(Ac)_2$ and $Ti(OBu)_4$ is 1:1; the mass ratio of PVP and $Ti(OBu)_4$ is 1:2]. The solution was stirred for ~6 hours at room temperature. The spinning process was the same as that for the TiO_2 sponge. The obtained sponge was then treated at a heating rate of 2°C/min and a holding time of 1 hour at 750°C in air and then cooled in the furnace.

Characterization and mechanical testing

The weight of the sponge was measured by an electronic balance with an accuracy of 0.01 mg. The dimensions of macroscopic specimens were determined via a vernier caliper with an accuracy of 0.02 mm, whereas the dimensions of microscopic specimens were measured optically by a field emission SEM (LEO-1530, Zeiss). The microstructure of specimens was observed using the same SEM. A TEM (JEOL-2010) operating at 120 kV was used to obtain TEM images and determine the mean grain size of nanofibers in the sponges. The crystalline structure was identified by using x-ray diffraction (XRD; D/max-2500, Rigaku) with Cu Kα radiation at a scanning rate of 0.5 and 7°/min with 2θ ranging from 20° to 80°.

In situ monotonic and cyclic compressive tests on TiO_2 sponges at room temperature and 400°C were conducted at a constant displacement rate of 10 μm/s via Hysitron PI 85 PicoIndenter inside an SEM (Quanta FEG 450), and high temperature was achieved via a MEMS heating device integrated in the thermal module of PI 85. Compressive testing on ZrO_2 sponges at 400°, 600°, and 800°C was performed at a constant displacement rate of 40 μm/s via Hysitron TI 950 TriboIndenter with a temperature control stage. During the experiments of photocatalytic activity of TiO_2 sponges, the dyed sponge was irradiated by simulated solar light (SEX300c, Perfectlight) with an electricity of 16 A and a distance of 22 cm.

SUPPLEMENTARY MATERIALS

Supplementary material for this article is available at http://advances.sciencemag.org/cgi/content/full/3/6/e1603170/DC1

fig. S1. Photograph of the experimental setup.
fig. S2. Diameter of TiO_2 fibers at different concentrations of PVP.
fig. S3. Structural characterization of ZrO_2 nanofiber sponge.
fig. S4. Structural characterization of YSZ nanofiber sponge.
fig. S5. Structural characterization of $BaTiO_3$ nanofiber sponge.
fig. S6. Room temperature compression and recovery of different ceramic nanofiber sponges.
fig. S7. An Ashby plot of compressive modulus versus relative density to compare the present ceramic sponge with different foams and aerogels.
fig. S8. In situ SEM cyclic compression of TiO_2 nanofiber sponge.
fig. S9. Compressive testing of TiO_2 nanofiber sponge.
fig. S10. Compression and recovery of ceramic nanofiber sponges heated with the flame of an alcohol lamp.
fig. S11. Temperature distribution in the methane flame used in this work.
fig. S12. Compressive stress-strain curves of YSZ nanofiber sponge at 400° and 600°C.
fig. S13. XRD data of TiO_2 calcined at 450°and 650°C.
fig. S14. TEM images of TiO_2 nanofibers after calcining at 650°C.
fig. S15. Cyclic compressive stress-strain curves for 10 cycles of a TiO_2 nanofiber sponge calcined at 650°C.

fig. S16. Hydroscopicity of TiO_2 nanofiber sponge.
fig. S17. A TiO_2 nanofiber sponge, which absorbed methylene blue solution was compressed and then recovered after being released.
fig. S18. Temperature raising on the top surface of a ZrO_2 nanofiber sponge and other materials on a 400°C heating stage.
table S1. The densities and thermal conductivities of ZrO_2 nanofiber sponge and other thermal insulation materials.
movie S1. Room temperature compression and recovery of TiO_2, ZrO_2, and $BaTiO_3$ nanofiber sponges.
movie S2. In situ SEM compressive testing of a TiO_2 nanofiber sponge.
movie S3. Compressive testing of macroscopic TiO_2 nanofiber sponge for 100 cycles.
movie S4. Compression of TiO_2, ZrO_2, and $BaTiO_3$ nanofiber sponges in an alcohol flame.
movie S5. In situ SEM compressive of a TiO_2 nanofiber sponge at 400°C.
movie S6. Compression and recovery of YSZ nanofiber sponge in a high-temperature methane flame.
movie S7. YSZ nanofiber sponge maintaining elasticity after cyclic compression in the methane flame.
References (*35*–*46*)

REFERENCES AND NOTES

1. L. Qiu, J. Z. Liu, S. L. Chang, Y. Wu, D. Li, Biomimetic superelastic graphene-based cellular monoliths. *Nat. Commun.* **3**, 1241 (2012).
2. C. Zhu, T. Y.-J. Han, E. B. Duoss, A. M. Golobic, J. D. Kuntz, C. M. Spadaccini, M. A. Worsley, Highly compressible 3D periodic graphene aerogel microlattices. *Nat. Commun.* **6**, 6962 (2015).
3. H. Bi, I.-W. Chen, T. Lin, F. Huang, A new tubular graphene form of a tetrahedrally connected cellular structure. *Adv. Mater.* **27**, 5943–5949 (2015).
4. L. J. Gibson, M. F. Ashby, *Cellular Solids: Structure and Properties* (Cambridge Univ. Press, 1999).
5. T. A. Schaedler, A. J. Jacobsen, A. Torrents, A. E. Sorensen, J. Lian, J. R. Greer, W. B. Carter, Ultralight metallic microlattices. *Science* **334**, 962–965 (2011).
6. X. Zheng, W. Smith, J. Jackson, B. Moran, H. Cui, D. Chen, C. M. Spadaccini, Multiscale metallic metamaterials. *Nat. Mater.* **15**, 1100–1106 (2016).
7. A. C. Pierre, G. M. Pajonk, Chemistry of aerogels and their applications. *Chem. Rev.* **102**, 4243–4266 (2002).
8. J. L. Mohanan, I. U. Arachchige, S. L. Brock, Porous semiconductor chalcogenide aerogels. *Science* **307**, 397–400 (2005).
9. F. Menaa, A. Abdelghani, B. Menaa, Graphene nanomaterials as biocompatible and conductive scaffolds for stem cells: Impact for tissue engineering and regenerative medicine. *J. Tissue Eng. Regener. Med.* **9**, 1321–1338 (2015).
10. H. Bi, X. Xie, K. Yin, Y. Zhou, S. Wan, L. He, R. S. Ruoff, Spongy graphene as a highly efficient and recyclable sorbent for oils and organic solvents. *Adv. Funct. Mater.* **22**, 4421–4425 (2012).
11. S. Pathak, E. J. Lim, P. Pour Shahid Saeed Abadi, S. Graham, B. A. Cola, J. R. Greer, Higher recovery and better energy dissipation at faster strain rates in carbon nanotube bundles: An in-situ study. *ACS Nano* **6**, 2189–2197 (2012).
12. H. Sun, Z. Xu, C. Gao, Multifunctional, ultra-flyweight, synergistically assembled carbon aerogels. *Adv. Mater.* **25**, 2554–2560 (2013).
13. M. Sternitzke, Structural ceramic nanocomposites. *J. Eur. Ceram. Soc.* **17**, 1061–1082 (1997).
14. Z. C. Eckel, C. Zhou, J. H. Martin, A. J. Jacobsen, W. B. Carter, T. A. Schaedler, Additive manufacturing of polymer-derived ceramics. *Science* **351**, 58–62 (2016).
15. D. Jang, L. R. Meza, F. Greer, J. R. Greer, Fabrication and deformation of three-dimensional hollow ceramic nanostructures. *Nat. Mater.* **12**, 893–898 (2013).
16. H. C. Cao, E. Bischoff, O. Sbaizero, M. Rühle, A. G. Evans, D. B. Marshall, J. J. Brennan, Effect of interfaces on the properties of fiber-reinforced ceramics. *J. Am. Ceram. Soc.* **73**, 1691–1699 (1990).
17. X. Zheng, H. Lee, T. H. Weisgraber, M. Shusteff, J. DeOtte, E. B. Duoss, J. D. Kuntz, M. M. Biener, Q. Ge, J. A. Jackson, S. O. Kucheyev, N. X. Fang, C. M. Spadaccini, Ultralight, ultrastiff mechanical metamaterials. *Science* **344**, 1373–1377 (2014).
18. J. Bauer, S. Hengsbach, I. Tesari, R. Schwaiger, O. Kraft, High-strength cellular ceramic composites with 3D microarchitecture. *Proc. Natl. Acad. Sci. U.S.A.* **111**, 2453–2458 (2014).
19. L. R. Meza, S. Das, J. R. Greer, Strong, lightweight, and recoverable three-dimensional ceramic nanolattices. *Science* **345**, 1322–1326 (2014).
20. J. F. Poco, J. H. Satcher Jr., L. W. Hrubesh, Synthesis of high porosity, monolithic alumina aerogels. *J. Non-Cryst. Solids* **285**, 57–63 (2001).
21. G. Zu, J. Shen, X. Wei, X. Ni, Z. Zhang, J. Wang, G. Liu, Preparation and characterization of monolithic alumina aerogels. *J. Non-Cryst. Solids* **357**, 2903–2906 (2011).
22. S. O. Kucheyev, T. F. Baumann, C. A. Cox, Y. M. Wang, J. H. Satcher Jr., A. V. Hamza, J. E. Bradby, Nanoengineering mechanically robust aerogels via control of foam morphology. *Appl. Phys. Lett.* **89**, 041911 (2006).
23. B. J. Clapsaddle, B. Neumann, A. Wittstock, D. W. Sprehn, A. E. Gash, J. H. Satcher Jr., M. Bäumer, A sol–gel methodology for the preparation of lanthanide-oxide aerogels: Preparation and characterization. *J. Sol-Gel Sci. Technol.* **64**, 381–389 (2012).
24. J. Chen, X. Liao, M. Wang, Z. Liu, J. Zhang, L. Ding, Y. Li, Highly flexible, nonflammable and free-standing SiC nanowire paper. *Nanoscale* **7**, 6374–6379 (2015).
25. A. Biswas, H. Park, W. M. Sigmund, Flexible ceramic nanofibermat electrospun from TiO_2–SiO_2 aqueous sol. *Ceram. Int.* **38**, 883–886 (2012).
26. Y. Si, J. Yu, X. Tang, J. Ge, B. Ding, Ultralight nanofibre-assembled cellular aerogels with superelasticity and multifunctionality. *Nat. Commun.* **5**, 5802 (2014).
27. D. Li, Y. Xia, Fabrication of titania nanofibers by electrospinning. *Nano Lett.* **3**, 555–560 (2003).
28. E. S. Medeiros, G. M. Glenn, A. P. Klamczynski, W. J. Orts, L. H. C. Mattoso, Solution blow-spinning: A new method to produce micro- and nanofibers from polymer solutions. *J. Appl. Polym. Sci.* **113**, 2322–2330 (2009).
29. C. Ferraro, E. Garcia-Tuñon, V. G. Rocha, S. Barg, M. D. Fariñas, T. E. G. Alvarez-Arenas, G. Sernicola, F. Guiliani, E. Saiz, Light and strong SiC networks. *Adv. Funct. Mater.* **26**, 1636–1645 (2016).
30. D. P. Hashim, N. T. Narayanan, J. M. Romo-Herrera, D. A. Cullen, M. G. Hahm, P. Lezzi, J. R. Suttle, D. Kelkhoff, E. Muñoz-Sandoval, S. Ganguli, A. K. Roy, D. J. Smith, R. Vajtai, B. G. Sumpter, V. Meunier, H. Terrones, M. Terrones, P. M. Ajayan, Covalently bonded three-dimensional carbon nanotube solids via boron induced nanojunctions. *Sci. Rep.* **2**, 363 (2012).
31. A. H. Landrock, *Handbook of Plastic Foams: Types, Properties, Manufacture, and Applications* (Noyes Publications, 1995).
32. A. Cao, P. L. Dickrell, W. G. Sawyer, M. N. Ghasemi-Nejhad, P. M. Ajayan, Super-compressible foamlike carbon nanotube films. *Science* **310**, 1307–1310 (2005).
33. J. Bauer, A. Schroer, R. Schwaiger, O. Kraft, Approaching theoretical strength in glassy carbon nanolattices. *Nat. Mater.* **15**, 438–443 (2016).
34. R. Asahi, T. Morikawa, T. Ohwaki, K. Aoki, Y. Taga, Visible-light photocatalysis in nitrogen-doped titanium oxides. *Science* **293**, 269–271 (2001).
35. G. Zu, J. Shen, L. Zou, W. Wang, Y. Lian, Z. Zhang, A. Du, Nanoengineering super heat-resistant, strong alumina aerogels. *Chem. Mater.* **25**, 4757–4764 (2013).
36. R. W. Pekala, C. T. Alviso, J. D. Lemay, Organic aerogels: Microstructural dependence of mechanical-properties in compression. *J. Non-Cryst. Solids* **125**, 67–75 (1990).
37. M. A. Worsley, S. O. Kucheyev, J. H. Satcher Jr., A. V. Hamza, T. F. Baumann, Mechanically robust and electrically conductive carbon nanotube foams. *Appl. Phys. Lett.* **94**, 073115 (2009).
38. J. Zou, J. Liu, A. S. Karakoti, A. Kumar, D. Joung, Q. Li, S. I. Khondaker, S. Seal, L. Zhai, Ultralight multiwalled carbon nanotube aerogel. *ACS Nano* **4**, 7293–7302 (2010).
39. T. M. Tillotson, L. W. Hrubesh, Transparent ultralow-density silica aerogels prepared by a two-step sol-gel process. *J. Non-Cryst. Solids* **145**, 44–50 (1992).
40. T.-Y. Wei, T.-F. Chang, S.-Y. Lu, Y.-C. Chang, Preparation of monolithic silica aerogel of low thermal conductivity by ambient pressure drying. *J. Am. Ceram. Soc.* **90**, 2003–2007 (2007).
41. S. Zhao, Z. Zhang, G. Sèbe, R. Wu, R. V. Rivera Virtudazo, P. Tingaut, M. M. Koebel, Multiscale assembly of superinsulating silica aerogels within silylated nanocellulosic scaffolds: Improved mechanical properties promoted by nanoscale chemical compatibilization. *Adv. Funct. Mater.* **25**, 2326–2334 (2015).
42. X. Jia, B. Dai, Z. Zhu, J. Wang, W. Qiao, D. Long, L. Ling, Strong and machinable carbon aerogel monoliths with low thermal conductivity prepared via ambient pressure drying. *Carbon* **108**, 551–560 (2016).
43. G. S. Kim, S. H. Hyun, Effect of mixing on thermal and mechanical properties of aerogel-PVB composites. *J. Mater. Sci.* **38**, 1961–1966 (2003).
44. J. He, X. Li, D. Su, H. Ji, Y. Qiao, High-strength mullite fibers reinforced ZrO2–SiO2 aerogels fabricated by rapid gel method. *J. Mater. Sci.* **50**, 7488–7494 (2015).
45. J. He, X. Li, D. Su, H. Ji, X. Wang, Ultra-low thermal conductivity and high strength of aerogels/fibrous ceramic composites. *J. Eur. Ceram. Soc.* **36**, 1487–1493 (2016).
46. C.-Q. Hong, J.-C. Han, X.-H. Zhang, J.-C. Du, Novel nanoporous silica aerogel impregnated highly porous ceramics with low thermal conductivity and enhanced mechanical properties. *Scr. Mater.* **68**, 599–602 (2013).

Acknowledgments

Funding: This work was supported by the National Basic Research of China (grant nos. 2015CB932500 and 2013CB632702), the National Natural Science Foundation of China (grant nos. 51302141, 51272037, 51272126, and 11522218), and Program for New Century Excellent Talents in University (grant no. NCET-12-0097). H. Wu and X.L. acknowledge support from the 1000 Youth Talents Plan of China. H.G. acknowledges support from the National Science

Foundation (grant CMMI-1634492). **Author contributions:** H. Wu, X.L., H.G., and N.W. designed the research. H. Wang synthesized and characterized the specimens. X.Z. and Y.L. performed mechanical testing. H. Wang, X.Z., X.L., H. Wu, and H.G. wrote the paper. All authors analyzed the data, discussed the results, and commented on the manuscript. **Competing interests:** The authors declare that they have no competing financial interests. **Data and materials availability:** All data needed to evaluate the conclusions in the paper are present in the paper and/or the Supplementary Materials. Additional data related to this paper may be requested from the authors.

Submitted 14 December 2016
Accepted 13 April 2017
Published 2 June 2017
10.1126/sciadv.1603170

Citation: H. Wang, X. Zhang, N. Wang, Y. Li, X. Feng, Y. Huang, C. Zhao, Z. Liu, M. Fang, G. Ou, H. Gao, X. Li, H. Wu, Ultralight, scalable, and high-temperature–resilient ceramic nanofiber sponges. *Sci. Adv.* **3**, e1603170 (2017).